

## LOCAL PROPERTIES OF WMAP COLD SPOT

WEN ZHAO

Key Laboratory for Researches in Galaxies and Cosmology, University of Science and Technology of China, Hefei, 230026, China  
Niels Bohr Institute and DISCOVERY Center, Blegdamsvej 17, 2100 Copenhagen, Ø, Denmark

*Draft version June 4, 2019*

### ABSTRACT

We investigate the local properties of WMAP Cold Spot (CS) localized at ( $l = 209^\circ, b = -57^\circ$ ) in Galactic Coordinate by defining the local statistics: mean temperature, variance, skewness and kurtosis. Comparing with the Gaussian random simulations, as well as the other spots in WMAP data, we find that the local mean temperatures around CS are quite lower in the scale of  $R \lesssim 5^\circ$  as expected. In particular, we also find that the values of local variance and skewness around CS are all systematically larger in the scale of  $R > 5^\circ$ , which implies that WMAP CS is prefer a large-scale non-Gaussian structure to a combination of some small structures. The non-Gaussianity of CS is totally encoded in the WMAP low multipoles at  $l \leq 40$ . We also find that the cosmic texture can excellently explain all the excesses in these statistics. So the local analysis of the WMAP CS supports the cosmic texture explanation.

*Subject headings:* cosmic microwave background radiation — early universe — methods: data analysis  
— methods: statistical

### 1. INTRODUCTION

Cosmic Microwave Background (CMB) radiation is one of the most ancient fossils of the Universe. The observations of the NASA Wilkinson Microwave Anisotropy Probe (WMAP) satellite on the CMB temperature and polarization anisotropies have put tight constraints on the cosmological parameters (Komatsu et al. 2011). In addition, some anomalies in CMB field have also been reported soon after the release of the WMAP data (see (Bennett et al. 2011) as a review). Among these, an extremely Cold Spot (CS) centered at the position ( $l = 209^\circ, b = -57^\circ$ ) and a characteristic scale about  $10^\circ$  in the Galactic Coordinate was detected in the Spherical Mexican Hat Wavelet (SMHW) non-Gaussian analysis (Vielva et al. 2004).

Comparing with the distribution derived from the isotropic and Gaussian CMB simulations, due to this CS, the SMHW coefficients of WMAP data have an excess of kurtosis (Cruz et al. 2005). In addition, several non-Gaussian statistics, such as the amplitude and area of the cold spot, the higher criticism and so on, have also been applied to identify this WMAP CS (Cruz et al. 2007a, 2005; Cayon et al. 2005; Naselsky et al. 2010; Zhang & Huterer 2010; Vielva 2010). Since then, various alternative explanations for the CS have been proposed, including the possible foregrounds (Cruz et al. 2006; Hansen et al. 2012), Sunyaev-Zeldovich effect (Cruz et al. 2008), the supervoid in the Universe (Inoue & Silk 2006, 2007; Inoue 2012), and the cosmic texture (Cruz et al. 2007b, 2008). At the same time, some analyses have been carried out to distinguish these explanations, such as the non-Gaussian tests for the different detectors and different frequency channels of WMAP satellite (Vielva et al. 2004; Cruz et al. 2005), the investigation of the NVSS sources (Rudnick et al. 2007; Smith & Huterer 2010), the survey around the CS with MegaCam on the Canada-France-Hawaii Telescope (Granett et al. 2009), the redshift survey using VIMOS on VLT towards CS (Bremer et al. 2010), and the cross-

correlation between WMAP and Faraday depth rotation map (Hansen et al. 2012).

Due to the fact that, nearly all the explanations of CS are related to the local characters of the CMB field, the studies on the local properties of CS are necessary. In this paper, we shall propose a set of novel non-Gaussian statistics, i.e. the local mean temperature, variance, skewness and kurtosis, to study the local properties of the CMB field. By altering the radius of the cap around CS, we study the local properties of CS at different scales. We find that different from the general properties of the foregrounds, the point sources or various local contaminations, in the small scales the local variance, skewness and kurtosis values of CS are not significantly large, except for its coldness in temperature. However, after the careful comparison with Gaussian simulations, as well as the other spots in the WMAP field, we find that when  $R > 5^\circ$  the local variance and skewness are systematically large. This suggests that CS is prefer a large-scale non-Gaussian structure to a combination of some small structures. In order to confirm it, we repeat the analyses adopted by many authors, where the statistics of temperature and kurtosis in SMHW domain are used. We apply these analyses to the WMAP data with different  $l_{\max}$ , and find that nearly all the non-Gaussianities of CS are encoded in the low multipoles  $l \leq 40$ .

It was claimed that the cosmic texture seems to be most promising among all the explanations (Cruz et al. 2007b, 2008), by investigating the temperature and area of CS. In order to check this explanation by our local statistics, we add a similar cosmic texture into the Gaussian simulations, and calculate the local quantities of CMB fields. We find that the excesses of the local statistics of WMAP CS can be excellently explained by this non-Gaussian structure. So our local analysis of the CS supports the cosmic texture explanation.

The rest of the paper is organized as follows: In Section 2, we introduce the WMAP data, which will be used in the analysis. In Section 3, we define the local statistics

and apply them into WMAP data. In Section 4, the non-Gaussianities of CS is studied for the WMAP data with different  $l_{\text{max}}$ , which shows that the non-Gaussian signals are all encoded in the low multipoles. Section 5 summarizes the main results of this paper.

## 2. THE WMAP DATA AND SIMULATIONS

In our analysis, we shall use the WMAP data including the QVW7 map, ILC7 map and the NILC5 map.

### 2.1. QVW7

The CMB temperature maps derived from the WMAP observations are pixelized in HEALPix format with the total number of pixels  $N_{\text{pix}} = 12N_{\text{side}}^2$ . In our analysis, we use the 7-year WMAP data for Q, V and W frequency bands with  $N_{\text{side}} = 512$ . The linearly co-added map (written as ‘‘QVW7’’) is constructed using an inverse weight of the pixel-noise variance  $\sigma_0^2/\bar{N}_{\text{obs}}$ , where  $\sigma_0$  denotes the pixel noise for each differential assembly (DA) and  $\bar{N}_{\text{obs}}$  represents the full-sky average of the effective number of observations for each pixel.

### 2.2. ILC7 and NILC5

The WMAP instrument is composed of 10 DAs spanning five frequencies from 23 to 94 GHz (Bennett et al. 2003). The internal linear combination (ILC) method has been used by WMAP team to generate the WMAP ILC maps (Hinshaw et al. 2007; Gold et al. 2011). The 7-year ILC (written as ‘‘ILC7’’) map is a weighted combination from all five original frequency bands, which are smoothed to a common resolution of one degree. For the 5-year WMAP data, in (Delabrouille et al. 2009) the authors have made a higher resolution CMB ILC map (written as ‘‘NILC5’’), an implementation of a constrained linear combination of the channels with minimum error variance on a frame of spherical called needlets<sup>1</sup>. In this paper, we will also consider both these two maps for the analysis. Note that all these WMAP data have the same resolution parameter  $N_{\text{side}} = 512$ , and the corresponding total pixel number  $N_{\text{pix}} = 3145728$ .

In comparison with WMAP observations to give constraint on the statistics, a  $\Lambda$ CDM cosmology is assumed with the cosmological parameters given by the WMAP 7-year best-fit values (Komatsu et al. 2011):  $100\Omega_b h^2 = 2.255$ ,  $\Omega_c h^2 = 0.1126$ ,  $\Omega_\Lambda = 0.725$ ,  $n_s = 0.968$ ,  $\tau = 0.088$  and  $\Delta_{\mathcal{R}}^2(k_0) = 2.430 \times 10^{-9}$  at  $k_0 = 0.002\text{Mpc}^{-1}$ . We simulate the CMB maps for each frequency channel by considering the WMAP beam resolution and instrument noise, and then co-add them with inverse weight of the full-sky averaged pixel-noise variance in each frequency to get the simulated QVW7 maps. Similar to the previous work (Hansen et al. 2012), to simulate the ILC7 maps, we ignore the noises and smooth the simulated map with one degree resolution. And for NILC5, we consider the noise level and beam window function given in (Delabrouille et al. 2009). In all the simulations, we assumed that the temperature fluctuations and instrument noise follow the Gaussian distribution, and do not consider any effect due to the residual foreground contaminations.

<sup>1</sup> The similar map for 7-year WMAP data is recently gotten in (Basak & Delabrouille 2011).

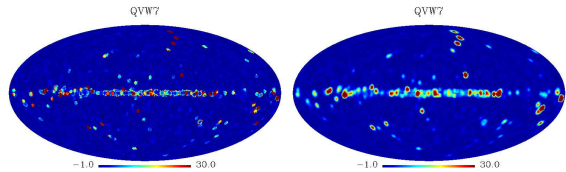


**Figure 1.** The  $K(R)$  (left) and  $\bar{K}(R)$  (right) maps for QVW7 data. In both map, we have adopted  $R = 2^\circ$ .

## 3. LOCAL STATISTICS OF THE CMB FIELD

### 3.1. Local statistics

In this section, we shall investigate the local properties of the CMB field, especially the WMAP Cold Spot, by using the local statistics: mean temperature, variance, skewness and kurtosis.

The statistics of local skewness and kurtosis were firstly introduced in (Bernui & Reboucas 2009). For a given WMAP data with  $N_{\text{side}} = 512$  (QVW7, ILC7 or NILC5), we degrade it to the lower resolution  $N_{\text{side}} = 256$  to reduce the effect of the noises. And then, for this degraded CMB map, the constructive process can be formalized as follows. Let  $\Omega(\theta_j, \phi_j; R)$  be a spherical cap with an aperture of  $R$  degree, centered at  $(\theta_j, \phi_j)$ . We can define the functions  $M$  (mean temperature),  $V$  (standard deviation),  $S$  (skewness) and  $K$  (kurtosis) that assign to the  $j^{\text{th}}$  cap, centered at  $(\theta_j, \phi_j)$  by the following way:

$$\begin{aligned} M_j(R) &= \frac{1}{N_p} \sum_{i=1}^{N_p} T_i, \\ V_j(R) &= \left( \frac{1}{N_p} \sum_{i=1}^{N_p} T_i^2 \right)^{1/2}, \\ S_j(R) &= \frac{1}{N_p V_j^3} \sum_{i=1}^{N_p} T_i^3, \\ K_j(R) &= \frac{1}{N_p V_j^4} \sum_{i=1}^{N_p} T_i^4 - 3, \end{aligned} \quad (1)$$

where  $N_p$  is the number of pixels in the  $j^{\text{th}}$  cap,  $T_i$  is the temperature at  $i^{\text{th}}$  pixel. Obviously, the values  $S_j$  and  $K_j$  obtained in this way for each cap can be viewed as a measure of non-Gaussianity in the direction of the center of the cap  $(\theta_j, \phi_j)$ . For a given aperture  $R$ , we can scan the celestial sphere with evenly distributed spherical caps, and build the  $M(R)$ -,  $V(R)$ -,  $S(R)$ -,  $K(R)$ -maps. In our analysis, we have chosen the locations of centroids of spots to be the pixels in  $N_{\text{side}} = 64$  resolution. By choosing different  $R$  values, one can study the local properties of the CMB field at different scales. In (Bernui & Reboucas 2009, 2010, 2012), the statistics  $S_j(R)$  and  $K_j(R)$  with large  $R$  values have been applied to study the large-scale globe non-Gaussianity in the CMB field. However, in this paper we shall apply them to study the CMB local properties.

It is important to mention that these definitions cannot well localize the non-Gaussian sources. For example, in Fig. 1 the kurtosis map  $K(R)$  (left panel), we can find the clear circular morphology around the point

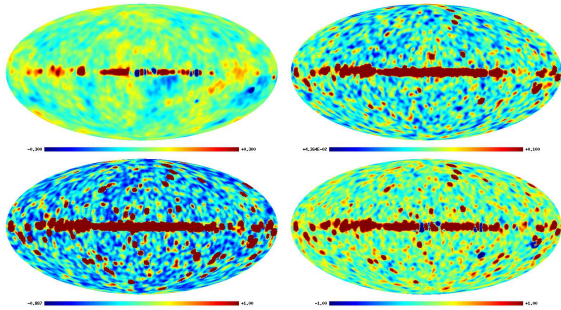


**Figure 2.** Closewise,  $\bar{M}(R)$  map,  $\bar{V}(R)$  map,  $\bar{S}(R)$  map and  $\bar{K}(R)$  map for QVW7, where  $R = 2^\circ$ . Note that the  $\bar{M}(R)$  and  $\bar{V}(R)$  maps have the unit: mK.

sources. This means that the values of  $K_j$  always maximize/minimize at the edge of the circles, rather than the center of the circles. To overcome this problem and localize the non-Gaussian sources, it is better to define the following average quantities,

$$\bar{X}_j(R) = \frac{1}{N_p} \sum_{j=1}^{N_p} X_j(R), \quad (2)$$

where  $X = M, V, S, K$  for mean temperature, standard deviation, skewness and kurtosis.  $X_j$  is the corresponding local quantities defined above, and  $N_p$  is again the number of pixels in the  $j^{\text{th}}$  cap. For the comparison, we plot the corresponding  $\bar{K}(R)$  in the right panel of Fig. 1.

Now, let us apply the method to the CMB maps. Firstly, we consider the QVW7 map. By choosing  $R = 2^\circ$ , we plot  $\bar{X}(R)$  maps in Fig. 2. The figures clearly show that these local statistics are sensitive to the foreground residuals and various point sources. From  $\bar{M}$ -map, one finds that most non-Gaussianity comes from the Galactic plane around  $b = 0^\circ$ . However, from  $\bar{V}$ -,  $\bar{S}$ - and  $\bar{K}$ -maps, various extra point sources far from the Galactic plane are clearly presented.

Similarly, we also apply the method to the ILC7 and NILC5 maps by choosing  $R = 2^\circ$ . The results are shown in Fig. 3 and Fig. 4. We find that these ILC maps are much cleaner than QVW7 map in all the four  $\bar{M}$ -,  $\bar{V}$ -,  $\bar{S}$ -,  $\bar{K}$ -maps. Even so, from the  $\bar{V}$ -,  $\bar{S}$ -,  $\bar{K}$ -maps, we still find some non-Gaussian sources in the Galactic plane. In addition, two obvious sources at  $(l = 209.5^\circ, b = 20.1^\circ)$  and  $(l = 184.9^\circ, b = 5.98^\circ)$  are clearly localized in ILC7 map, which have been identified as the known point sources, and masked in the KQ75y7 mask (Gold et al. 2011).

### 3.2. The local properties of WMAP Cold Spot

In this subsection, we shall focus on the local statistics for WMAP Cold Spot at  $(l = 209^\circ, b = -57^\circ)$  in Galactic Coordinate. First, for a given  $\bar{X}(R)$  map ( $R = M, V, S$  or  $K$ ), we compare the values centered at CS with those of other spots. From Fig. 2, we can find in the maps derived from QVW7 data, there are too many point sources even in the outside of the Galactic plane. So, for a fair comparison, in this subsection we shall only consider the ILC7 and NILC5 maps.

To quantify the properties of CS, we define the proba-

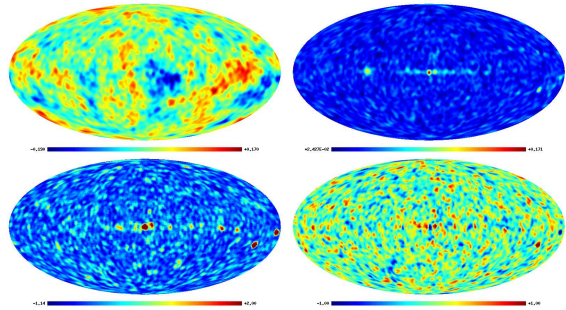


**Figure 3.** Closewise,  $\bar{M}(R)$  map,  $\bar{V}(R)$  map,  $\bar{S}(R)$  map and  $\bar{K}(R)$  map for ILC7, where  $R = 2^\circ$ . Note that the  $\bar{M}(R)$  and  $\bar{V}(R)$  maps have the unit: mK.

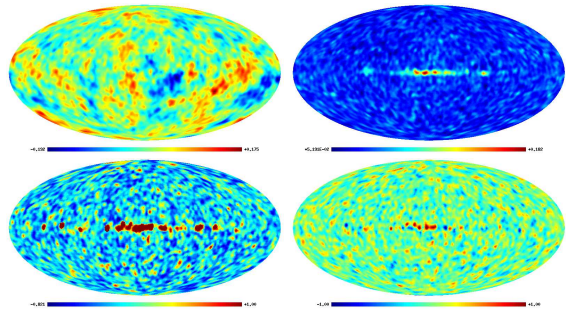


**Figure 4.** Closewise,  $\bar{M}(R)$  map,  $\bar{V}(R)$  map,  $\bar{S}(R)$  map and  $\bar{K}(R)$  map for NILC5, where  $R = 2^\circ$ . Note that the  $\bar{M}(R)$  and  $\bar{V}(R)$  maps have the unit: mK.

bility  $p$ -value as follows,

$$\begin{aligned} p &= \text{Prob}(x_i < x_0), \text{ for } \bar{M}(R), \\ p &= \text{Prob}(x_i > x_0), \text{ for } \bar{V}(R), \\ p &= \text{Prob}(|x_i| > |x_0|), \text{ for } \bar{S}(R), \bar{K}(R), \end{aligned} \quad (3)$$

where  $x_i$  are the values of  $\bar{X}$  for spots in the region of  $|b| > 30^\circ$ , and  $x_0$  is that for CS. Note that in our analysis, the Galactic plane with  $|b| < 30^\circ$  has been excluded to reduce the contamination of foreground residuals. So for the mean temperature maps, a smaller  $p$ -value indicates a colder spot of CS, and for the  $\bar{V}(R)$  maps, a smaller  $p$ -value shows that the variance around CS is larger than the other spots. While for  $\bar{S}(R)$  and  $\bar{K}(R)$  maps, smaller  $p$ -values suggest the larger non-Gaussianities around CS. As we can imagine that if CS is simply cold without any non-Gaussianity, the  $p$ -values for  $\bar{V}$ -,  $\bar{S}$  and  $\bar{K}$  should be normal, i.e. close to 0.5. On the other hand, if CS is a combination of some small-scale non-Gaussian structures, as some explanations in (Cruz et al. 2006), the local variance, skewness and kurtosis in small scales should be quite large. However, as we will show below, none of these is the case of WMAP CS.

We plot the  $p$ -values as functions of  $R$  in Fig. 5 for both ILC7 (solid lines) for NILC5 (dashed lines). From both cases, as anticipated we find that the CS is very cold comparing with other spots in WMAP data, i.e.  $p < 10^{-3}$  for  $R < 5^\circ$ . Especially, when  $R = 2^\circ, 3^\circ, 4^\circ$ , we have  $p = 0$ , i.e. CS is the coldest spot in the considered region of WMAP data. However, as  $R$  increases, the  $p$ -value also increases. In particular, when  $R \geq 10^\circ$ , we find  $p > 0.1$ , i.e. CS becomes a normal spot.

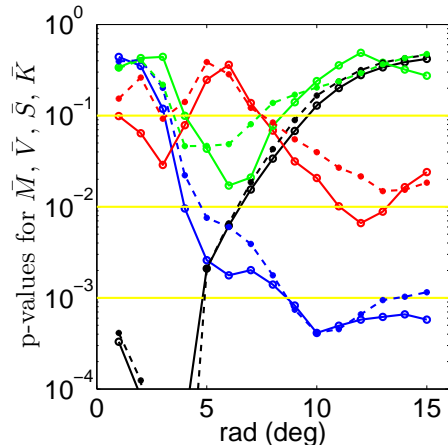


**Figure 5.** The p-values for ILC7 (solid lines) and NILC5 (dashed lines). Black lines are for  $\bar{M}$ , blue ones are for  $\bar{V}$ , red ones are for  $\bar{S}$ , and green ones are for  $\bar{K}$ .

For the  $\bar{V}$  maps, the situation is different: the  $p$ -values decrease with the increasing of  $R$ . When  $R < 5^\circ$ , we find  $p > 0.01$ , i.e. CS is quite normal comparing with other spots. But, when  $R$  is larger than  $10^\circ$ ,  $p < 10^{-4}$  is always holden. Similar results are also obtained in the  $\bar{S}$  maps. Although it is less significant, we also find that local skewness of CS is systematically larger than the other spots in the large scale, i.e.  $R > 10^\circ$ . Meanwhile, Fig. 5 also shows that the local kurtosis is quite normal in all the scales  $1^\circ \leq R \leq 15^\circ$ .

In order to cross-check these results, we can also compare WMAP CS with the random Gaussian simulations. To do it, we consider 500 random Gaussian samples, and calculate the values of  $\bar{X}(R)$  at the spot ( $l = 209^\circ, b = -57^\circ$ ) for each realization. In Figs. 6 and 7, we plot mean values and corresponding error bars of the local statistics of these realizations and compare them with the WMAP results. From these figures, we find the similar results as in Fig. 5: When  $R < 5^\circ$ , the WMAP CS is quite colder than the simulations. While in the cases with  $R > 5^\circ$ , the local variance and skewness values are systematically larger.

Combining these results, we find that WMAP Cold Spot seems to prefer a nontrivial large-scale structure to a combination of some small non-Gaussian structures (for instance, the point sources or foreground residuals, which always follows the non-Gaussianity in the small scales as shown in Fig. 2). This is one of the main conclusions in this paper.

### 3.3. Comparing with simulation including cosmic texture

In (Cruz et al. 2007b, 2008), by studying the temperature and area of CS, the authors found that the cosmic texture, rather than the other explanations, provides an excellent interperation for the WMAP Cold Spot<sup>2</sup>. In this subsection, we shall study if the local anomalies of CS found in this work is consistent with the cosmic texture explanation.

<sup>2</sup> In the review paper (Vielva 2010), one can find some other explanations, and the corresponding criticisms, which will not be considered in this paper.

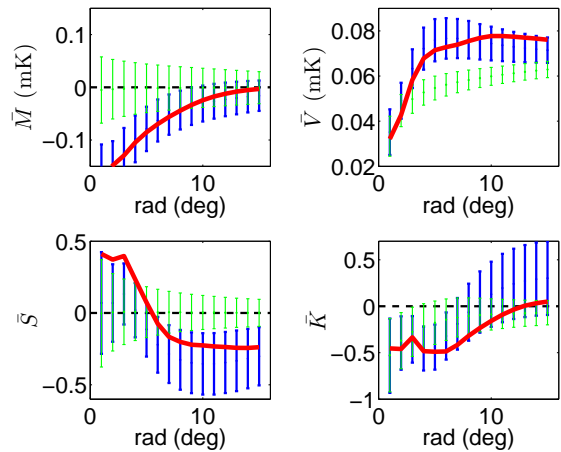


**Figure 6.** The values of statistics for ILC7 compare with 500 simulations. Red lines denote the WMAP results. Blue ones indicate the average values and the corresponding error bars of simulations in the case with cosmic texture, and green ones are for the case without cosmic texture.

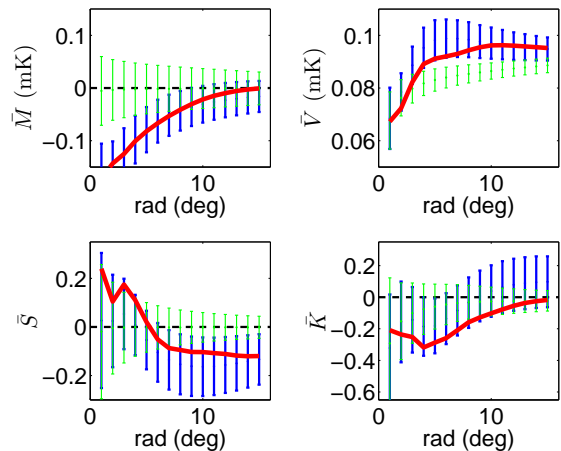


**Figure 7.** The values of statistics for NILC5 compare with 500 simulations. Red lines denote the WMAP results. Blue ones indicate the average values and the corresponding error bars of simulations in the case with cosmic texture, and green ones are for the case without cosmic texture.

The profile for the CMB temperature fluctuation caused by a collapsing cosmic texture is given by

$$\frac{\Delta T}{T} = - \begin{cases} \frac{\varepsilon}{\sqrt{1+4(\frac{\vartheta}{\vartheta_c})^2}} & \text{if } \vartheta \leq \vartheta_* \\ \frac{\varepsilon}{2} e^{-\frac{1}{2\vartheta_c^2}(\vartheta^2 + \vartheta_*^2)} & \text{if } \vartheta > \vartheta_* \end{cases} \quad (4)$$

where  $\vartheta$  is the angle from the center.  $\varepsilon$  is the amplitude parameter, and  $\vartheta_c$  is the scale parameter.  $\vartheta_* = \sqrt{3}/2\vartheta_c$ . By the Bayesian analysis, the texture parameters were obtained  $\varepsilon = 7.3_{-3.6}^{+2.5} \times 10^{-5}$  and  $\vartheta_c = 4.9_{-2.4}^{+2.8}$  deg at 95% confidence (Cruz et al. 2007b).

In our calculation, we adopt the best-fit texture parameters  $\varepsilon = 7.3 \times 10^{-5}$  and  $\vartheta_c = 4.9^\circ$ . In above discussion, we have compared the WMAP CS with 500 Gaussian simulations. Here, in order to taking into account the cosmic texture, for each realization we add the texture morphology at the same position ( $l = 209^\circ, b = -57^\circ$ ),



**Table 1**  
For ILC7, the  $\chi^2$  for various statistics

	$\chi_M^2$	$\chi_V^2$	$\chi_S^2$	$\chi_K^2$	$\chi_{tot}^2$
without texture	35.16	43.27	31.83	10.46	120.73
with texture	34.01	29.04	12.76	7.40	83.21

**Table 2**  
For NILC5, the  $\chi^2$  for various statistics

	$\chi_M^2$	$\chi_V^2$	$\chi_S^2$	$\chi_K^2$	$\chi_{tot}^2$
without texture	33.67	36.23	43.24	13.54	126.68
with texture	31.17	25.27	19.82	11.03	87.29

and then repeat the exactly same analyses as in the previous subsection. The results are also shown in Figs. 6 and 7 (blue dots and error bars). Interestingly enough, we find that WMAP CS is exactly consistent with the simulations if the cosmic texture is considered. For each statistic with every  $R$  value, the value of WMAP CS is equal to the mean value of simulations in  $1\text{-}\sigma$  confident level. The cosmic texture can excellently account for the excesses of  $\bar{M}$ ,  $\bar{V}$  and  $\bar{S}$  of WMAP CS.

In order to quantify it, we calculate the  $\chi^2$  for each statistic as follows

$$\chi_Y^2 = \sum_{R_i, R_j} (Y_0(R_i) - \bar{Y}(R_i)) \Sigma_{ij}^{-1} (Y_0(R_j) - \bar{Y}(R_j)), \quad (5)$$

where  $Y = \bar{M}, \bar{V}, \bar{S}, \bar{K}$ .  $R_i$  and  $R_j$  run through  $1^\circ$  to  $15^\circ$ .  $Y_0(R_i)$  are the values of the statistics for WMAP CS, and  $Y(R_i)$  are those for the simulations.  $\bar{Y}(R_i)$  is average value of  $Y(R_i)$ .  $\Sigma$  is the covariance matrix of the vector  $Y(R_i)$ . The total value can also be defined as  $\chi_{tot}^2 = \chi_M^2 + \chi_V^2 + \chi_S^2 + \chi_K^2$ .

For both cases (ILC7 and NILC5) with and without cosmic texture, we list the  $\chi_Y^2$  values in Table 1 and 2. From both tables, we find that once the cosmic texture is considered in simulations, comparing with the pure Gaussian samples, every  $\chi_Y^2$  value reduces, especially for  $Y = \bar{V}$  and  $Y = \bar{S}$ . So we conclude that the local analysis of WMAP CS strongly supports the cosmic texture explanation.

#### 4. COLD SPOT AND WMAP LOW MULTIPOLES

If WMAP Cold Spot is a large-scale non-Gaussian structure as we have found in previous section by the local analysis, the non-Gaussianity caused by CS should be encoded in the low multipoles rather than the high multipoles. In this section, we shall confirm it by studying the effect of different multipoles on the WMAP non-Gaussian signals.

Following (Vielva et al. 2004; Cruz et al. 2005, 2006; Zhang & Huterer 2010), in this section we study the non-Gaussianity of WMAP data by using the wavelet transform, which can emphasis or amplify some features of the CMB data at a particular scale. The Spherical Mexican Hat Wavelets are defined as

$$\Psi(\theta; R) = A(R) \left(1 + \left(\frac{y}{2}\right)^2\right) \left(2 - \left(\frac{y}{2}\right)^2\right) e^{-y^2/2R^2}, \quad (6)$$

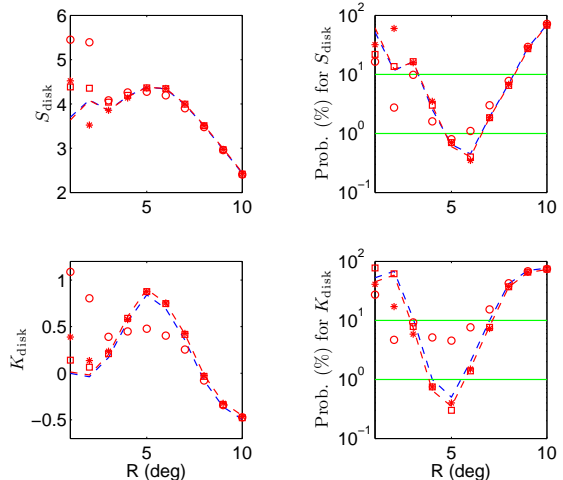


**Figure 8.** Values and probabilities of the statistics  $S_{\text{disk}}$  (upper) and  $K_{\text{disk}}$  (lower) for various cases. In all panels, the blue lines are for the results of QVW7 map, and red lines are for ILC7 map. The circles are for the ILC7 with  $l_{\text{max}} = 20$ , the crosses are for that with  $l_{\text{max}} = 40$ , and the squares are for that with  $l_{\text{max}} = 100$ .

where  $y \equiv 2 \tan(\theta/2)$  is the stereographic projection variable, and  $\theta \in [0, \pi)$  is the co-latitude.  $R$  is the scale, and  $A$  is the constant for the normalization, which can be written as

$$A(R) = \left[2\pi R^2 \left(1 + \frac{R^2}{2} + \frac{R^4}{4}\right)\right]^{-1/2}. \quad (7)$$

The continuous wavelet transform stereographically projected over the sphere with respect to  $\Psi(\theta; R)$  is given by

$$T_w(\hat{r}; R) = \int d\Omega' T(\hat{r} + \hat{r}') \Psi(\theta'; R), \quad (8)$$

where  $\hat{r} = (\theta, \phi)$  and  $\hat{r}' = (\theta', \phi')$  are the stereographic projections to sphere of center of the spot and the dummy location, respectively. In our analysis in this section, the locations of centroids of spots are chosen to be centers of pixels in  $N_{\text{side}} = 32$  resolution. Following (Zhang & Huterer 2010), we define the occupancy fraction as follows to account for the masked parts of the sky,

$$N_w(\hat{r}; R) = \int d\Omega' M(\hat{r} + \hat{r}') \Psi^2(\theta'; R), \quad (9)$$

where  $M(\hat{r})$  is KQ75y7 mask (Gold et al. 2011). In order to reduce the biases due to masking, we only include the results for spot locations  $\hat{r}$  for which  $N_w(\hat{r}; R) > 0.95$ .

In our analysis in this section, we shall consider the QVW7 and ILC7 data. We degrade them to a lower resolution with  $N_{\text{side}} = 128$ , then apply the KQ75y7 mask. For each masked WMAP data, we use the SMHW transform in Eq. (8) to get the corresponding map in wavelet domain  $T_w(\hat{r}; R)$ . To investigate the non-Gaussianity in different scales, for each map we consider the cases with  $R = 1^\circ, 2^\circ, 3^\circ, 4^\circ, 5^\circ, 6^\circ, 7^\circ, 8^\circ, 9^\circ, 10^\circ$ . Similar to many authors (Vielva et al. 2004; Cruz et al. 2005, 2006; Zhang & Huterer 2010), we define the statistics  $S_{\text{disk}}$  and  $K_{\text{disk}}$  as follows to study the non-Gaussianity related

to WMAP CS:

$$S_{\text{disk}}(R) = \frac{T_{\text{w}}^{\text{coldest}}(\hat{r}; R)}{\sigma_{\text{w}}(R)}, \quad (10)$$

$$K_{\text{disk}}(R) = \frac{1}{N_{\text{spots}}} \frac{\sum_{i=1}^{N_{\text{spots}}} T_{\text{w}}^4(\hat{r}_i; R)}{\sigma_{\text{w}}^4(R)} - 3. \quad (11)$$

Here  $\sigma_{\text{w}}(R)$  is the standard deviation of the distribution of all spots in a given map, and  $T_{\text{w}}^{\text{coldest}}(\hat{r}, R)$  is the coldest spot in this distribution. From the definitions, we find that  $S_{\text{disk}}(R)$  describes the cold spot significance, and  $K_{\text{disk}}(R)$  is the kurtosis of spots in a given map. In Fig. 8 (left panels), we present the values of  $S_{\text{disk}}(R)$  and  $K_{\text{disk}}(R)$  for different scale parameter  $R$ . Both QVW7 and ILC7 illustrate the same results: the values of both  $S_{\text{disk}}(R)$  and  $K_{\text{disk}}(R)$  maximize at  $R \sim 5^\circ$ . The results then compare with 2000 randomly generated Gaussian simulations, with the exactly same methodology applied. So we can get the probabilities of simulations, which have the larger  $S_{\text{disk}}(R)$  or  $K_{\text{disk}}(R)$  than those of WMAP data. These probabilities for both statistics are also shown in Fig. 8 (right panel). So, similar to other works (Vielva et al. 2004; Cruz et al. 2005; Zhang & Huterer 2010), we find that when  $R = 4^\circ - 6^\circ$ , WMAP data have the deviations from the Gaussian simulations, i.e. the corresponding probabilities for the statistics  $S_{\text{disk}}(R)$  and/or  $K_{\text{disk}}(R)$  are smaller than 1%.

Now, let us study which multipoles account for the non-Gaussianity above. We consider the original ILC7 map  $T(\hat{r})$ , and expand it via spherical harmonic composition:

$$T(\hat{r}) = \sum_{l,m} a_{lm} Y_{lm}(\hat{r}), \quad (12)$$

where  $Y_{lm}$  are the spherical harmonics and  $a_{lm}$  are the corresponding coefficients. Then the new map can be constructed as follows:

$$T'(\hat{r}) = \sum_{l=2}^{l_{\text{max}}} \sum_{m=-l}^l a_{lm} Y_{lm}(\hat{r}). \quad (13)$$

It is clear that this new map only includes the low multipoles  $l \in [2, l_{\text{max}}]$ . Thus, we can repeat the steps above by using the ILC7 map  $T'(\hat{r})$  instead of  $T(\hat{r})$ . In the analysis, we choose three cases with  $l_{\text{max}} = 20$ ,  $l_{\text{max}} = 40$  and  $l_{\text{max}} = 100$  to study the effect of different multipoles, and show the results in Fig. 8 with *circles*, *crosses* and *squares*, respectively. We find that for the statistic  $S_{\text{disk}}(R)$ , even only the low multipoles  $l \leq 20$  are considered, the values of the statistic and the corresponding probabilities are quite close to those gotten in the map including all the multipoles. These clearly show that the coldness of CS are mainly encoded in these lowest multipole range, which is consistent with the conclusion in (Naselsky et al. 2010). While for the statistic  $K_{\text{disk}}(R)$ , we find the WMAP data are quite normal for the case with  $l_{\text{max}} = 20$ , comparing with the Gaussian simulations. However, if  $l_{\text{max}} = 40$  is considered, the results for both statistics are very close to those in the map with all multipoles. So we conclude that WMAP CS reflects directly the peculiarities of the low multipoles  $l \leq 40$ , which suggests that CS should be a large-scale non-Gaussian structure, rather than a combination of

some small structures. This is consistent with our conclusion in Section 3.

## 5. CONCLUSION

Since the discovery of non-Gaussian Cold Spot in WMAP data, it has attracted much attention, and many explanations have been proposed. To distinguish them, in this paper we have studied the local properties of WMAP CS at different scales by introducing the local statistics including the mean temperature, variance, skewness and kurtosis. Comparing with the other spots in WMAP data, as well as those in the Gaussian random simulations, we found the excesses of local variance and skewness in the large scale at  $R > 5^\circ$ , rather than in the small scales. At the same time, we found that the non-Gaussianity caused by CS is totally encoded in the WMAP low multipoles  $l \leq 40$ . These all imply that WMAP CS is prefer a large-scale non-Gaussian structure to a combination of some small structures.

It was claimed by many authors that the cosmic texture with a characteristic scale about  $10^\circ$ , rather than other mechanisms, could provide the excellent explanation for WMAP CS. By comparing with the random simulations including the similar texture structure, we found this non-Gaussian structure can excellently explain the excesses of the local variance and skewness, in addition to the coldness of WMAP CS. So our results in this paper strongly support the cosmic texture explanation.

We appreciate useful discussions with P. Naselsky, J. Kim, M. Hansen and A.M. Frejsel. We acknowledge the use of the Legacy Archive for Microwave Background Data Analysis (LAMBDA). Our data analysis made the use of HEALPix (Gorski et al. 2005) and GLESP (Doroshkevich et al. 2005). This work is supported by NSFC No. 11173021 and 11075141.

## REFERENCES

- Basak, S. & Delabrouille, J. 2011, arXiv:1106.5383  
 Bennett, C. L. et al., 2003, ApJS, 148, 1  
 Bennett, C. L. et al., 2011, ApJS, 192, 17  
 Bernui, A. & Reboucas, J. J. 2009, Phys. Rev. D, 79, 063528  
 Bernui, A. & Reboucas, J. J. 2010, Phys. Rev. D, 81, 063533  
 Bernui, A. & Reboucas, J. J. 2012, Phys. Rev. D, 85, 023522  
 Bremer, M. N., Silk, J., Davies L. J. M. & Lehnert, M. D. 2010, MNRAS, 404, L69  
 Cayon, L., Lin, J. & Treaster, A. 2005, MNRAS, 362, 826  
 Cruz, M., Martinez-Gonzalez, E., Vielva, P. & Cayon, L. 2005, MNRAS, 356, 29  
 Cruz, M., Tucci, M., Martinez-Gonzalez, E. & Vielva, P. 2006, MNRAS, 369, 57  
 Cruz, M., Cayon, L., Martinez-Gonzalez, E. & Vielva, P. 2007, ApJ, 655, 11  
 Cruz, M., Turok, N., Vielva, P., Martinez-Gonzalez, E. & Hobson, M. P. 2007, Science, 318, 1612  
 Cruz, M., Martinez-Gonzalez, E., Vielva, P., Diego, J. M., Hobson, M. & Turok, N. 2008, MNRAS, 390, 913  
 Delabrouille, J., Cardoso, J. F., Le Jeune, M., Betoule, M., Fay, G. & Guilloux, F. 2009, A&A, 493, 835  
 Doroshkevich, A. G., Naselsky, P. D., Verkhodanov, O. V., Novikov, D. I., Turchaninov, V. I., Novikov, I. D., Christensen, P. R. & Chiang, L. -Y. 2005, International Journal of Modern Physics D, 14, 275  
 Gold, B. et al., 2011, ApJS, 192, 15  
 Gorski, K. M., Hivon, E., Banday, A. J., Wandelt, B. D., Hansen, F. K., Reinecke, M. & Bartelman, M. 2005, ApJ, 622, 759  
 Granett, B. R., Szapudi, I. & Neyrinck, M. C. 2009, ApJ, 714, 825  
 Hansen, M., Zhao, W., Frejsel, A. M., Naselsky, P. D., Kim, J. & Verkhodanov, O. V. 2012, arXiv:1202.1711  
 Hinshaw, G. et al., 2007, ApJS, 170, 288  
 Inoue, K. T. & Silk, J. 2006, ApJ, 648, 23

- Inoue, K. T. & Silk, J. 2006, *ApJ*, 664, 650  
Inoue, K. T. 2012, *MNRAS*, 421, 2731  
Komatsu, E. et al., 2011, *ApJS*, 192, 18  
Naselsky, P. D., Christensen, P. R., Coles, P., Verkhodanov, O.,  
Novikov, D. & Kim, J. 2010, *Astrophys. Bull.*, 65, 101  
Rudnick, L., Brown, S. & Williams, L. R. 2007, *ApJ*, 671 40  
Smith, K. M. & Huterer, D. 2010, *MNRAS*, 403, 2  
Vielva, P., Martinez-Gonzalez, E., Barreiro, R. B., Sanz, J. L. &  
Cayon, L. 2004, *ApJ*, 609, 22  
Vielva, P. 2010, arXiv:1008.3051  
Zhang, R. & Huterer, D. 2010, *Astroparticle Physics*, 33, 69